THE ASTROPHYSICAL JOURNAL, 380:124–139, 1991 October 10

THE STELLAR CONTENT AND STRUCTURE OF THE GLOBULAR CLUSTER NGC 5053

GREGORY G. FAHLMAN,[1] HARVEY B. RICHER,[1] AND JAMES NEMEC[1]
Department of Geophysics and Astronomy, 2219 Main Hall, University of British Columbia Vancouver, BC, Canada V6T 1Z4
Received 1991 January 22; accepted 1991 April 23

ABSTRACT

Five overlapping fields in the metal poor globular cluster NGC 5053 have been observed with the CCD system at the Canada-France-Hawaii Telescope. The data have been used used to obtain deep star counts, $V \leq 25.0$, covering an east-west strip extending through the cluster center to close to the tidal radius. From the star counts alone, we determine a minimum mass–to–visual light ratio of $\mathcal{M}/L_V = 0.68 \pm 0.07$. This estimate is independent of kinematical observations and dynamical models of the cluster structure.

The stellar luminosity functions at different radial positions within the cluster were converted to the corresponding mass functions using a 16 Gyr oxygen-enhanced isochrone of metallicity [Fe/H] = -2.03. Mass segregation is observed. For a mass function of the form $n(m) \propto m^{-(1+x)}$, we find that the core of the cluster has $x \simeq 0.8$, whereas the outer region has $x \simeq 2.0$. The global luminosity function for the stars with $V \leq 23.5$ corresponds very well to a mass function with $x = 1.5$. The degree of mass segregation is broadly consistent with the predictions of multimass King models appropriate to NGC 5053. However, the observed mass segregation itself does not appear to provide a useful constraint on the amount of dark matter in the cluster.

The projected mass and number density profiles for the cluster have been fitted with a series of representative multimass King models. Given that our surface brightness profile has a peculiarly high value (compared with an isotropic King model) in the most distant annulus defined in our study, we cannot conclusively rule out the possibility that the cluster may have an anisotropic velocity distribution that extends inside the cluster core. The recently determined value for the velocity dispersion of the cluster giants, together with our global mass function, leads to a global mass–to–visual-light ratio of $\mathcal{M}/L_V \approx 1.2$. This result, which is based on a multimass King model, implies that the cluster main-sequence mass function must be fairly abruptly truncated at the observational limit of our data, i.e., $m \simeq 0.35\ m_\odot$.

Finally we present a new color-magnitude diagram for NGC 5053 which reaches $V = 23.5$, well below the main-sequence turn-off. From a comparison with the main-sequence fiducial of M92, we estimate the distance modulus and reddening of NGC 5053 to be $(m - M)_V = 16.08$ and $E(B - V) = 0.06$, respectively. This comparison also shows that NGC 5053 and M92 are the same age, independently of uncertainties in the distance moduli or reddenings of the clusters.

Subject headings: clusters: globular — luminosity function — stars: abundances — stars: evolution

1. INTRODUCTION

One of the most important new areas opened up by the use of CCD systems for globular cluster photometry is the study of faint main-sequence luminosity functions. There are at least two reasons for this interest: (1) the stellar mass spectrum has a significant effect on the dynamical evolution of globular clusters (e.g., Chernoff & Weinberg 1990; Murphy, Cohn, & Hut 1990), and (2) there appear to be real differences among the luminosity functions of different clusters (e.g., McClure et al. 1986), which may provide important constraints on star formation in the early stages of Galactic formation. The two issues are intertwined because dynamical evolution will lead to mass segregation, complicating the interpretation of observed luminosity functions, and to the preferential loss of low-mass stars, thereby altering the mass spectrum over time (Chernoff & Weinberg 1990; Lee, Fahlman, & Richer 1991). Mass segregation among main-sequence stars has been detected in M5 (Richer & Fahlman 1987), M30 (Richer, Fahlman, & VandenBerg 1988; Bolte 1989; Piotto et al. 1990), and M71 (Richer & Fahlman 1989). Evidence that the mass function may be altered in the course of dynamical evolution is presented in Richer et al. (1990).

NGC 5053 is of particular interest in this context. It has a low degree of central concentration; the concentration parameter $c = \log r_t/r_c$, where r_t and r_c are the tidal and core radius, respectively, is $c = 0.75$ (Peterson & King 1975), placing NGC 5053 among the most open of the Galactic globular clusters. This means that it is practical to observe faint main-sequence stars right at the center of the cluster. Hence one can obtain a rather complete stellar census of the entire cluster and obviate the need for detailed corrections due to mass segregation. The large core radius leads to a long dynamical time scale; e.g., Peterson & King (1975) calculate the central relaxation time to be 5.5×10^9 yr. From a dynamical point of view, NGC 5053 is young, and hence its observed mass function is expected to be close to the initial mass function (apart, of course, from the high-mass stars which have evolved over the lifetime of the cluster).

A further point of interest is the fact that NGC 5053 is very metal-poor. In the Zinn & West (1984) compilation, it is, with [Fe/H] = -2.58 (measured by Bell & Gustafsson 1983), the most metal-poor cluster listed. More recently, Suntzeff, Kraft, & Kinman (1988) observed six bright stars in NGC 5053 and obtained a mean metallicity of [Fe/H] = -2.2, a value equal to that of their lowest metallicity calibrating clusters M92 and

[1] Visiting Astronomer, Canada-France-Hawaii Telescope, which is operated by the National Research Council of Canada, the Centre National de la Recherche Scientifique of France, and the University of Hawaii.

M15. The interest in the metallicity derives from the apparent correlation between the slope of the main-sequence mass function and the metallicity discovered by McClure et al. (1986); i.e., lower metallicity clusters have a steeper mass function than higher metallicity clusters. If true, the result is surely of profound importance for Population II star formation. The correlation does remain even after simple mass segregation corrections are applied (Pryor, Smith, & McClure 1986); however, the validity of these corrections is somewhat questionable, since their King models were calculated for a restricted mass spectrum. NGC 5053 appears to be perhaps the best low-metallicity object available from the ground in which to obtain the global mass function directly. It would then provide an unambiguous limiting point for such a correlation.

It must be emphasized that the mass range on which the McClure et al. (1986) mass spectrum–metallicity correlation is based is quite restricted, typically extending from the main-sequence turnoff mass at around 0.8 $m_\odot$ to about 0.5 $m_\odot$. Recent observations made in the *I* band show that the main-sequence mass functions below about 0.4 $m_\odot$ in three nearby clusters appear to have a slope quite different from the slope observed at higher masses (Fahlman et al. 1989; Richer et al. 1990). Taken at face value, such results certainly cast doubt on the significance of any correlation established with only the most massive end of the mass function. Some caution is needed, however, because the mass-luminosity law needed to convert the observed star counts to a mass function is not yet well established at such low masses. Unfortunately only the very nearest clusters are close enough to permit photometric observations of the lower main sequence. With a distance modulus of about $(m - M)_V = 16.0$ (Sandage, Katem, & Johnson 1977, hereafter SKJ), NGC 5053 is certainly not among the systems accessible for such study.

As shown by Richer & Fahlman (1989) for M71, star counts as a function of radius may be used to infer the continuation of the mass function beyond the smallest observed mass if mass segregation is observed. Alternatively (or additionally), kinematical data may be used to estimate the gravitational mass, which may be compared with the luminous mass, thereby providing a handle on the dark (or merely dim) matter in the cluster (cf. Pryor et al. 1989). In practice both techniques involve comparing the cluster with multimass King models in order to determine parameters describing the mass in the cluster. Hence the structural parameters of the cluster, obtained from the radial surface brightness profile, are important.

In order to address the above issues, we obtained a set of deep CCD images in NGC 5053 designed to sample the entire radial extent of the cluster. The data are described in more detail in the following section. The discussion in this paper is limited to the visual star counts and their interpretation. We note that SKJ have published a color-magnitude diagram (CMD) for NGC 5053 which extends to just below the horizontal branch. Nemec & Cohen (1989), in the course of their study of the blue stragglers in NGC 5053, have published a deep CMD, reaching well below the main-sequence turnoff, for the Thuan-Gunn *g* and *r* colors. In view of this situation, a deep (V, $B-V$) CMD is presented in an appendix to this paper. A detailed discussion of our complete *UBV* photometry will be presented elsewhere.

2. OBSERVATIONS

A list of the observations used in this study is given in Table 1. All data were obtained at the prime focus of the Canada-France-Hawaii Telescope (CFHT) using an RCA CCD with 1024 × 640 15 μm pixels. The plate scale is 0".206 pixel^{-1}. The raw CCD frames were processed with the appropriate routines in IRAF, and the individual images of each field were added to produce a single image of the analysis discussed here. (The individual frames were also measured for the purpose of searching for low luminosity variable stars; Nemec et al. 1991.) The five fields define a strip beginning 1'.98 east of the cluster center and extend westward through the cluster center to a radius of 9'.45. The last two fields are at about the same radial distance from the cluster center. The geometry is sketched in Figure 1.

TABLE 1

NGC 5053 VISUAL EXPOSURES

Field	Time (s)	Seeing
1........	5 × 600	1".0
2........	5 × 600	0.9
3........	2 × 1800	0.8
4........	1800	0.8
5........	2 × 1800	0.9

The photometry was obtained using DAOPHOT (Stetson 1987). In brief, the threshold for finding stars was set about 3.5 σ, where σ is the standard deviation of the expected noise in a sky pixel. The basic procedure was as follows: (1) find and photometer stars on the image, (2) subtract the stars measured on the first pass to produce a residual image, (3) find and photometer stars on the residual image, (4) combine the star lists from steps 1 and 3 and use this as the input for the final

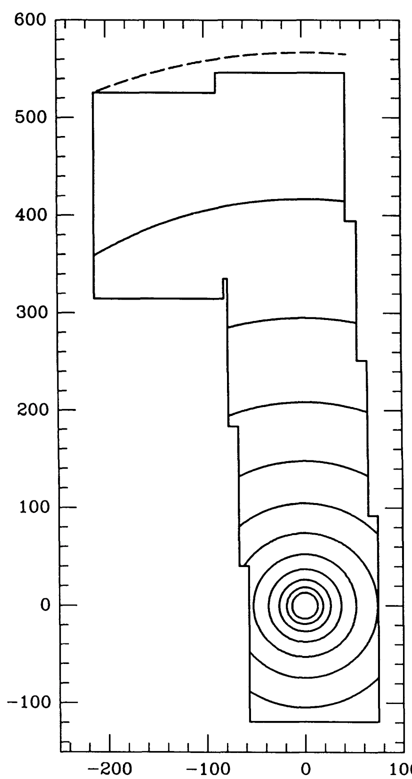

FIG. 1.—Schematic view of the CCD fields used in this study with the annulus boundaries shown. The scale along the two axes is in arcseconds, with the origin set on the cluster center as discussed in the text. West is at the top, and north is to the left.

photometry on the original image. Evidently such an iterative procedure can be continued, but after two passes, further gains are small. Compensation for the remaining stars was achieved through the completeness corrections discussed below.

Unfortunately, the entire observing run was plagued by light cirrus, and none of our data were obtained under photometric conditions. Thus, it was necessary to calibrate our data using the photoelectric and photographic photometry reported by SKJ. For this purpose, we used a 60 s visual image of the central region (field 1) and then transferred this calibration to the longer exposure frames listed in Table 1. The field 1 calibration was extended to the outer fields using the stars in the overlapped areas of the CCD images. The only uncertain calibration is between field 4 and field 5, where only five stars were identified in the small common area. In all other cases, a large number of stars were used to tie down the photometric zero points.

We identified 26 SKJ stars on our short frame but ended up using only 12 stars for the final calibration. Stars which DAOPHOT had trouble fitting, as indicated by the returned χ^2 statistic, were rejected, and we noted a systematic departure from a linear relation setting in at about $V = 17.0$, near the limit of the SKJ photometry. The 12 adopted standards are listed in Table 2. The adopted calibration is a simple offset, $v - V = \text{constant} \pm 0.07$, between the DAOPHOT estimate v and the SKJ magnitude V. For precise photometry, we should use a color term in the transformation. In practice the color coefficient for the CFHT RCA CCDs is small, typically of order 0.05 (see the CFHT CCD Observers Manual). Given that the color range of the stars to be counted here (in 0.5 mag bins) is about 0.6 mag, it is clear that neglecting the color term will not affect the results.

3. THE CLUSTER CENTER

Defining the center of a loose cluster like NGC 5053 is problematical at best, and the difficulty here is exacerbated by the limited spatial coverage of our data. Nemec & Cohen (1989) adopted a nominal center coinciding with a relatively bright and isolated star clearly shown in their Figure 6, a deep U image obtained at CFHT in the course of the observational program discussed here. Inspection of that picture makes the problem clear: the stars are almost uniformly distributed over the entire frame. After some experimentation, we decided to define the center of the cluster from the isopleths derived from the observed star counts in field 1. To the extent that the main-sequence stellar population is uniform in the core, these numbers should represent the mass distribution. A similar procedure was used in our analysis of the star counts in M71 (Richer & Fahlman 1989), another fairly loose cluster.

TABLE 2

PHOTOMETRIC CALIBRATION

SKJ	V SKJ	V FRN	Δ (FRN − SKJ)
C........	14.01	14.03	0.02
97........	15.06	15.05	−0.01
51........	15.24	15.14	−0.10
89........	15.44	15.51	0.07
84........	15.94	15.90	−0.04
25........	16.53	16.46	−0.07
55........	16.44	16.51	0.07
56........	16.58	16.55	−0.03
54........	16.63	16.63	0.00
57........	16.65	16.65	0.00
58........	16.68	16.82	0.14
99........	16.81	16.78	−0.03

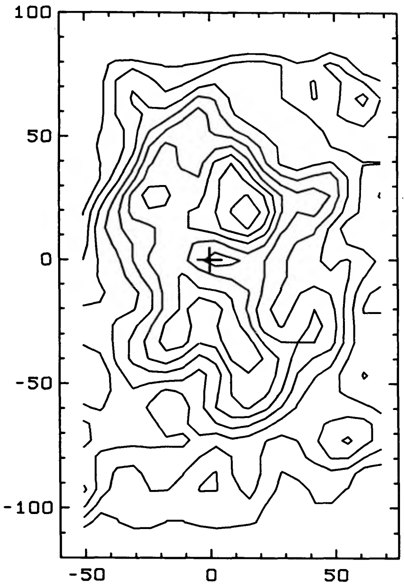

FIG. 2.—Contour plot showing the smoothed isopleths. The cross marks the centroid of the outermost complete contour which was adopted as the cluster center; see text for further details. The axes are marked in arcseconds, and the orientation is the same as in Fig. 1.

The stars were counted in square boxes 64 pixels on a side, placed on 32 pixel centers. The resulting 19 × 31 array of star numbers was subsequently convolved with a Gaussian of FWHM = 2.0 in order to produce reasonably smooth contours. The cluster center was defined as the centroid of the isopleth corresonding to 35 stars per box (about two-thirds of the peak value), which we judged to be representative of the overall symmetry of the cluster core. These isopleths are shown in Figure 2. The selected point turns out to be 3".2 north and 0".1 east of the Nemec-Cohen star and thus corresponds closely to the visually estimated cluster center.

As shown in Figure 2, our boxed and smoothed star counts have local maxima on either side of the cluster center, which, in turn, appears to be located in the local minimum. The other prominent star in this region, besides the Nemec-Cohen central star, is the second brightest blue straggler in the cluster (Nemec & Cohen 1989). A further curious feature of NGC 5053 is that the brightest stars are absent from the most central part of the cluster. With just a little imagination, they appear to be arranged in a partial ring beginning at a radius 1'.5 surrounding the cluster center. In this regard the wide-field photograph reproduced in SKJ (their Plate 1) is particularly striking. The physical significance, if any, of these points is decidedly unclear; however, the evident lumpiness of the stellar distribution in NGC 5053 does manifest itself in the surface density profile discussed later.

4. STAR COUNTS AND COMPLETENESS CORRECTIONS

The five fields were pieced together to form a continuous mosaic, which was then subdivided into a central region and 11 annuli (or sections of annuli) defined by projected radii spaced so that the area of successive complete annuli was doubled. The outer radius, area, and geometrical factor, g, needed to scale the observed section to a complete circular annulus are

TABLE 3

GEOMETRY OF THE ANNULI

Annulus (1)	Outer Radius (arcmin) (2)	Area (arcmin^2) (3)	Area Factor (4)	Effective Radius (arcmin) (5)	Mean Radius (arcmin) (6)
0........	0.220	0.152	1.0	0.156	0.161
1........	0.310	0.152	1.0	0.269	0.267
2........	0.483	0.301	1.0	0.380	0.377
3........	0.619	0.601	1.0	0.537	0.531
4........	0.875	1.199	1.0	0.758	0.754
5........	1.236	2.090	1.145	1.071	1.052
6........	1.746	2.717	1.757	1.512	1.482
7........	2.465	2.520	3.780	2.136	2.015
8........	3.482	2.327	8.166	3.017	2.923
9........	4.919	3.344	11.343	4.262	4.095
10.......	6.949	7.197	10.514	6.020	5.607
11.......	9.450	9.607	13.410	8.294	8.130

TABLE 4

COMPLETENESS CORRECTIONS

	FIELD 1					
	A0–A3		A3–A5		A5–A7	
V	Out/In	f	Out/In	f	Out/In	f
20.0–20.5.........	18/19	1.06	57/57	1.00	47/48	1.02
20.5–21.0.........	28/28	1.00	49/52	1.06	45/48	1.07
21.0–21.5.........	22/24	1.09	59/60	1.02	46/49	1.07
21.5–22.0.........	23/26	1.13	43/47	1.09	45/47	1.04
22.0–22.5.........	70/90	1.29	96/123	1.28	41/53	1.29
22.5–23.0.........	67/89	1.33	95/125	1.32	47/60	1.28
23.0–23.5.........	41/95	2.32	64/121	1.89	39/62	1.59

	FIELD 2			
	A3–A7		A7–A9	
V	Out/In	f	Out/In	f
22.0–22.5............	13/15	1.15	17/17	1.00
22.5–23.0............	19.23	1.26	33/33	1.00
23.0–23.5............	42/72	1.31	33/37	1.12
23.5–24.0............	33/65	1.97	56/94	1.68
24.0–24.5............	34/150	...	75/188	2.51

	Field 3		Field 4		Field 5	
V	Out/In	f	Out/In	f	Out/In	f
22.5–23.0.........	...	1.00	...	1.00	92/97	1.05
23.5–24.0.........	...	1.00	49/50	1.02	83/90	1.08
24.0–24.5.........	114/120	1.05	261/288	1.10	77/100	1.30
24.5–25.0.........	107/129	1.21	218/304	1.39	104/174	1.67
24.5–25.0.........	95/229	2.41	172/334	1.94	131/312	2.38

listed in columns (2)–(4) of Table 3. In that table we also list the effective radius, r_e, defined as the radius which bisects the area of the annulus, and the mean radius, r_*, of the observed objects brighter than $V = 23.5$. These two estimates for the characteristic radius of the stars in the annulus are in close agreement. In the subsequent discussion of the surface brightness distribution, we will adopt r_e as the radius corresponding to the surface brightness of the annulus in question, but, evidently, there would be little effect on the results if r_* were used instead.

The observed star counts must be corrected for the effects of incompleteness—due primarily to crowding in the inner regions and to sky noise in the outer fields. These correction factors were estimated by adding scaled replicas of the point-spread function to the data frames and then reducing the data as described earlier. Typically the number of stars added to a given frame was limited to about 10% of the number counted to avoid unduly altering the stellar distribution. Consequently, a large number of trails was needed to build up statistically significant estimates of the completeness factors.

The results are listed in Table 4. In the case of the two inner fields, the stellar gradient is noticeable, and we have partitioned the frames according to the annuli defined in Table 3. The completeness factors listed are defined as the ratio of the number of stars found to the number added in that bin. The recovery criteria were a positional match with the added star and also a magnitude difference. For field 1, the difference between the input and output magnitudes had to satisfy $|\Delta V| < 0.75$. For all other fields, we adopted $|\Delta V| < 0.5$. The higher cutoff in field 1 reflects the larger photometric errors induced by the crowding and was needed to give a corrected luminosity function which, when convolved with the full completeness matrix defined in Drukier et al. (1988), agreed better with the observed star counts. A plot of $|\Delta V|$ against the input magnitude for field 1 is shown in Figure 3. At the faint end there is considerable intrinsic scatter caused by the crowding in the frame. A similar plot for the field 2 added stars is shown in Figure 4. The scatter is smaller, reflecting the less crowded stellar distribution and the somewhat better seeing. Note that there is a definite bias toward seeing a few stars much brighter than their input magnitudes. We inspected the location of all the identifications with $|\Delta V| > 0.5$ on the original image and verified that essentially all were contaminated or otherwise confused with "real" stars or CCD artifacts. In Figure 5 we show the results for fields 3, 4, and 5 together. Evidently there is little scatter except at the faintest magnitudes, which, in any case, have completeness factors so large that they were not used in the analysis. These three figures well illustrate the photometric degradation caused by stellar crowding.

After the observed star counts have been corrected for incompleteness, the contribution from noncluster objects which happen to be in the field must be subtracted. Contami-

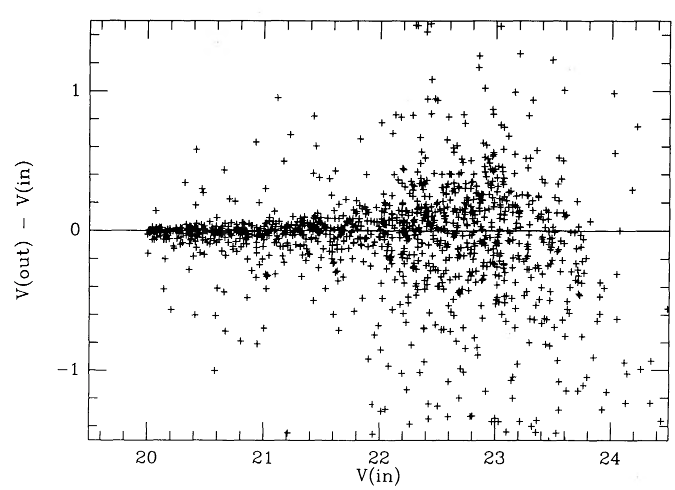

FIG. 3.—Photometric errors determined from artificial stars added in field 1. Here V(in) refers to the input magnitude and V(out) is the magnitude returned by DAOPHOT.

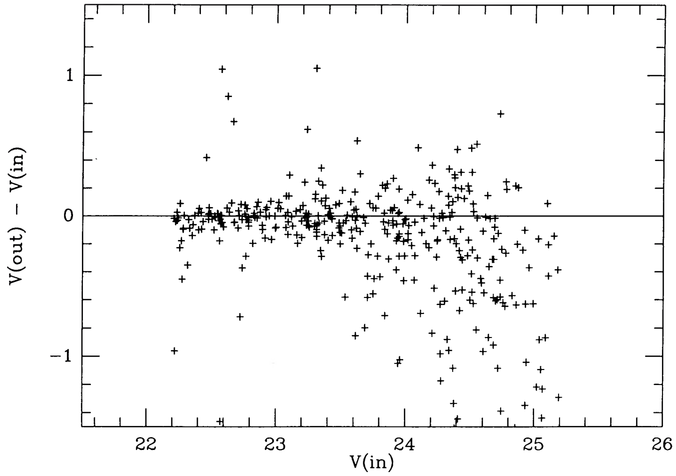

FIG. 4.—Photometric errors determined from artificial stars added to field 2.

nation by Galactic stars is unimportant because of the high Galactic latitude of NGC 5053, $b = 79°$ (cf. Ratnatunga & Bahcall 1985). However, there is certainly going to be a significant contribution from background galaxies which will be particularly important in the outer annuli. We were unable to obtain observations of a background field near the cluster, but we did obtain a deep exposure in a field at $b = 36°$. This exposure was made to search for an optical counterpart to an unusual radio source being studied by our colleague T. K. Menon. The data have been analyzed by DAOPHOT following the procedures used for the cluster fields. In other words, even though most of the objects were faint galaxies, they are treated as stellar objects. The object counts for Menon's field are listed in Table 5. The last column is a calculated number using the formula given in Drukier et al. (1988), which, in turn, is based on the faint galaxy counts of Tyson (1988). The agreement between the calculated estimate and the observed counts is surprisingly good. Consequently we adopt the formula of Drukier et al. (1988) to estimate the contribution of faint galaxies to the counts in NGC 5053.

The corrected star counts for all our annuli are presented in Table 6. The error estimates include (1) the Poisson error

TABLE 5

BACKGROUND COUNTS

V	Observed Counts	f	Corrected Counts	Stars (RB)	Δ	Galaxies (calculated)
17–18........	1	1.00	1.0	0.8	0.2	0.4
18–19........	1	1.00	1.0	0.8	0.2	0.8
19–20........	2	1.00	2.0	1.5	0.5	1.7
20–21........	5	1.00	5.0	1.5	3.5	3.6
21–22........	9	1.0	9.0	2.6	6.4	7.9
22–23........	36	1.03	37.1	2.6	34.5	17.4
23–24........	43	1.13	48.6	3.6	45.0	38.0
24–25........	37	1.83	67.8	3.6	64.2	83.2

associated with the raw counts, (2) the uncertainty in the incompleteness factor, and (3) a fixed 25% error in the background galaxy corrections.

5. THE LUMINOSITY AND MASS OF NGC 5053

The integrated magnitude of the cluster may be estimated by simply adding the flux from the individual stars observed in each annulus and then correcting this total for geometrical incompleteness only, using the numbers in Table 3. Including all the stars with $V > 16.0$, we obtain a total apparent magnitude of $V_t = 9.91$. Adopting the SKJ distance modulus of $(m - M)_V = 16.03$, we then obtain $M_{V,t} = -6.12$. This estimate does not include the stars with $V < 16.0$. A list of bright stars is given by SKJ (their Tables 1 and 2). When we include the cluster members with $V < 16.0$ from their lists, the integrated magnitude is increased to $M_{V,t} = -6.36$. To the extent that the SKJ lists are complete and the cluster is spherically symmetric (i.e., our geometrical completeness factors are valid; see below), this number is our best estimate of what the integrated magnitude of the cluster would be as measured in the sky.

A slightly different estimate may be obtained by summing the flux from the corrected star counts in Table 6, assigning the bin mean magnitude to each star in the bin. Adding in the bright stars as above, we find $M_{V,t} = -6.43 \pm 0.10$, where the error corresponds to the tabulated error in the star counts. This is perhaps a better estimate of the integrated light of the cluster, since it does take into account the incompleteness due to crowding and the contribution of the background objects. The two estimates agree because the brighter stars dominate the integrated light, and they are not severely affected by incompleteness.

Each of the above estimates is a lower limit in the sense that the data do not extend quite to the tidal radius, nor do they include any light from stars fainter than those counted. These contributions are unlikely to amount to more than a few percent. A much larger correction applies if the cluster is indeed as flattened as measured by White & Shawl (1987). They found an axial ratio of 0.79, placing NGC 5053 among the most flattened globular clusters.

White & Shawl (1987) determined the major axis of the cluster to be at an equatorial position angle of 111°. This is close enough to the east-west orientation of our data strip to imply that our measurements pertain primarily to the major axis of the cluster. Evidently, then, the assumption that our data are sections of spherically symmetric annuli will lead to an overestimate of the integrated luminosity. A simple correction procedure is to multiply the geometrical completion factors g, which are listed in Table 3, by the axial ratio. (Clearly, only those annuli with $g > 1/0.79$ should be corrected.) This leads to

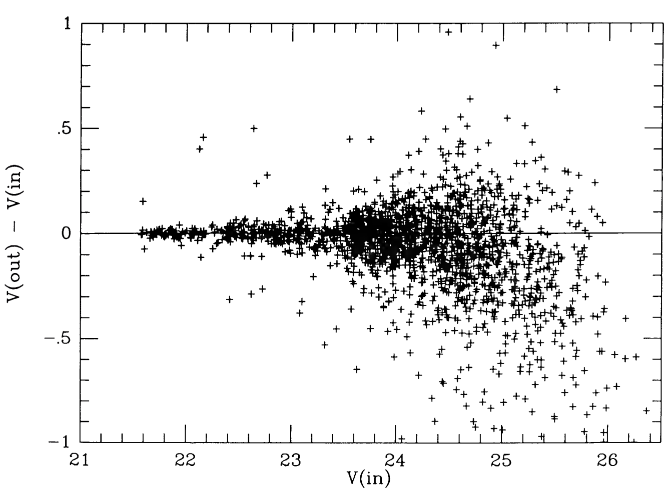

FIG. 5.—Photometric errors determined by artificial stars added to fields 3, 4, and 5.

TABLE 6

STAR COUNTS CORRECTED FOR COMPLETENESS AND BACKGROUND

V	A0		A1		A2		A3		A4		A5	
± 0.25	n_c	σ_n	n_c	σ_n	n_c	σ_n	n_c	σ_n	n_c	σ_n	n_c	σ_n
16.25........	0.0	0.0	1.0	1.0	0.0	0.0	0.0	0.0	1.0	1.0	0.0	0.0
16.75........	0.0	0.0	0.0	0.0	0.0	0.0	1.0	1.0	2.0	1.4	2.0	1.4
17.25........	0.0	0.0	0.0	0.0	1.0	1.0	2.0	1.4	1.0	1.0	0.0	0.0
17.75........	0.0	0.0	2.0	1.4	2.0	1.4	0.0	0.0	6.0	2.4	5.0	2.2
18.25........	3.0	1.7	0.0	0.0	2.0	1.4	3.0	1.7	9.0	3.0	1.0	1.0
18.75........	0.0	0.0	0.0	0.0	3.0	1.7	2.0	1.4	4.0	2.0	6.0	2.4
19.25........	3.0	1.7	9.0	3.0	8.0	2.8	8.0	2.8	19.0	4.4	18.0	4.3
19.75........	6.0	2.4	10.0	3.2	7.0	2.6	21.0	4.6	34.0	5.8	51.0	7.3
20.25........	7.4	2.8	7.4	2.8	17.9	4.5	32.7	6.1	58.0	7.6	72.0	8.5
20.75........	12.0	3.5	9.0	3.5	25.0	5.0	36.0	6.0	69.0	8.9	107	10.9
21.25........	10.9	3.5	17.5	4.5	16.4	4.3	59.8	8.8	99.7	10.2	141	12.0
21.75........	18.1	4.7	21.5	5.2	33.9	6.6	70.1	10.2	148	14.3	175	14.8
22.25........	27.0	6.1	41.1	4.3	47.6	8.3	81.0	11.2	155	15.9	239	20.3
22.75........	19.9	5.3	30.6	6.6	57.1	9.4	177	14.3	155	16.3	206	19.0
23.25........	13.9	5.9	32.4	9.5	57.9	13.4	116	21.3	223	28.1	211	23.7

V	A6		A7		A8		A9		A10		A11	
± 0.25	n_c	σ_n	n_c	σ_n	n_c	σ_n	n_c	σ_n	n_c	σ_n	n_c	σ_n
16.25........	1.0	1.0	1.0	1.0	4.0	2.0	2.0	1.4	1.0	1.0	0.0	0.0
16.75........	6.0	2.4	6.0	2.4	3.0	1.7	2.0	1.4	5.0	2.2	0.0	0.0
17.25........	5.0	2.2	1.0	1.0	2.0	1.4	1.0	1.0	0.0	0.0	0.0	0.0
17.75........	4.0	2.0	1.0	1.0	5.0	2.2	1.0	1.0	0.0	0.0	1.0	1.0
18.25........	5.0	2.2	4.0	2.0	4.0	2.0	1.0	1.0	1.0	1.0	0.0	0.0
18.75........	6.0	2.4	8.0	2.8	6.0	2.4	1.0	1.0	1.0	1.0	−0.6	0.0
19.25........	21.0	4.6	16.0	4.0	6.0	2.4	5.0	2.2	2.4	1.7	0.2	1.0
19.75........	52.0	7.2	41.0	6.4	17.0	4.1	10.0	3.2	3.1	2.0	−0.3	1.0
20.25........	72.5	8.7	53.4	7.3	22.0	4.7	9.4	3.2	5.6	2.6	5.1	2.6
20.75........	127	1.8	71.1	8.7	25.3	5.1	19.1	4.5	10.9	3.6	−0.7	1.6
21.25........	153	13.1	86.0	9.6	36.0	6.1	24.6	5.1	12.0	3.9	4.9	3.1
21.75........	189	14.3	102	10.3	48.5	7.0	39.0	6.4	14.5	4.4	7.0	3.9
22.25........	208	20.6	157	17.3	63.8	8.1	48.0	7.1	11.3	4.5	8.1	4.7
22.75........	288	25.4	133	15.9	77.8	9.0	40.6	6.8	23.7	6.3	25.0	7.1
23.25........	263	26.7	164	19.0	80.5	10.3	52.5	7.9	34.0	8.0	29.4	8.6
23.75........	306	55.1	231	35.9	124	15.8	72.5	9.8	41.2	10.1	49.9	12.3
24.25........	...	...	...	...	144	21.6	97.9	13.0	88.8	15.7	59.1	17.0
24.75........	...	...	...	...	...	...	121	22.2	158	25.4	145	28.2

an integrated magnitude, now corrected for the measured ellipticity, of $M_{V,t} = -6.19 \pm 0.10$. The error estimate is due solely to the uncertainty in the star counts; some additional uncertainty due to the crude nature of the ellipticity correction may apply.

The integrated magnitude tabulated by Webbink (1985) is only $M_{V,t} = -6.09$. Harris & Racine (1989) give $M_{V,t} = -6.20$, a value consistent with the photometry of Kron & Mayall (1960) and the distance modulus of SKJ. It is, of course, fortuitous that our revised estimate of the integrated magnitude is so close to the Kron-Mayall value. Nevertheless, it does lend credence to the White-Shawl ellipticity value. On the other hand, the magnitude based on spherical symmetry is not implausible, particularly given the difficulty of directly measuring the integrated magnitude of such a diffuse and extended object. Note that our data are unsuitable for obtaining an independent determination of the cluster ellipticity.

In what follows, we will assume spherical symmetry whenever geometrical corrections are called for. In practice this simply means that the geometrical completion factors listed in Table 3 are used without modification. Apart from the integrated magnitude and the total mass, which is discussed immediately below, this assumption has no important quantitative implications.

The total mass of the cluster was estimated by assigning a mean mass of the stars in each of the magnitude bins and then summing. For this purpose, we adopted the 16 Gyr isochrone calculated for the metal-poor cluster M68 (McClure et al. 1987). This isochrone is based on stellar models with an oxygen enhancement of [O/Fe] = 0.7, but the estimated cluster mass is quite insensitive to that detail.

The mean mass of each magnitude bin was obtained by integrating an $x = 1.5$ luminosity function (see the following section) over the bin. Assuming spherical symmetry, we estimate that the total mass of the luminous stars down to $V = 23.5$ is $\mathcal{M}_c(V < 23.5) = 11{,}621\ m_{\odot}$. To go to the fainter limit of $V = 25.0$, we must make a correction for the fact that these faint stars could not be detected within the central part of the cluster.

An inspection of Table 6 shows that the needed corrections are different for the three magnitude bins between $V = 23.5$ and $V = 25.0$. A very conservative approach is to assume that the mean surface density determined from the observed area is applicable to the unobserved area. Hence the counts need to be

TABLE 7

LUMINOSITY FUNCTIONS

	GLOBAL		INNER		OUTER	
V	N	σ_n	N	σ_n	N	σ_n
16.0–16.5........	74.5	26.0	2.0	1.2	24.2	19.8
16.5–17.0........	139	33.7	5.3	2.3	76.6	28.9
17.0–17.5........	44.8	17.5	4.0	2.0	11.9	11.9
17.5–18.0........	92.6	26.2	15.7	4.1	25.3	17.9
18.0–18.5........	97.1	24.7	18.1	4.3	22.4	15.9
18.5–19.0........	128	28.0	15.9	4.1	22.4	15.9
19.0–19.5........	301	44.2	67.6	8.4	87.2	34.7
19.5–20.0........	673	63.6	136	12.1	142	34.0
20.0–20.5........	954	77.9	206	15.3	239	58
20.5–21.0........	1314	91.2	273	17.8	341	68.9
21.0–21.5........	1735	109	364	21.1	484	84.1
21.5–22.0........	2315	130	492	27.5	709	103
22.0–22.5........	2877	156	598	33.2	797	115
22.5–23.0........	3318	179	616	35.0	1066	141
23.0–23.5........	3798	215	685	52.0	1374	171
23.5–24.0........	...	...	...	...	1962	228
24.0–25.0........	...	...	...	...	2887	321
25.0–25.5........	...	...	...	...	5038	533

corrected only by the ratio of observed to total area. In this way the total mass between $V = 23.5$ and $V = 25.0$ is found to be 7483 $m_\odot$. To put this number in perspective, we note that the stars in the observed area will contribute a total of 6302 $m_\odot$, so that the correction, in this case, is very small. A more realistic approach is to assume that the ratios of the global counts in adjacent bins have the values determined by the total counts in the outer, observed parts of the cluster. This procedure, which effectively accounts for the surface brightness profile, leads to a total mass between $V = 23.5$ and $V = 25.0$ of 11,573 $m_\odot$, i.e., about double the observed mass for those stars. This is likely to be somewhat of an overestimate because mass segregation will steepen the mass spectrum in the outer parts of the cluster. Other estimates for the total mass will be obtained later in the paper by making the more sophisticated assumption that the cluster structure follows a multimass King model. The results quoted here are model-independent.

From the above, we can calculate a lower limit to the cluster mass-to-light ratio, $\mathcal{M}/L_V$. Taking $M_{V,\odot} = 4.84$ and adopting $M_{V,t} = -6.40$, we find $\mathcal{M}/L_V = 0.68 \pm 0.07$, where the 10% uncertainty reflects the range resulting from the two mass correction estimates discussed above. This number, while perhaps unexciting, has the virtue of being independent of dynamical theory and kinematical observations; it depends only on the adopted stellar models. Note that this estimate of $\mathcal{M}/L_V$ includes only the luminous mass detected by our observations; it does not include any white dwarfs or neutron stars, nor does it include any contribution from low-mass stars below our magnitude limit.

6. THE MASS FUNCTION OF NGC 5053

A global luminosity function was constructed by summing the star counts over all annuli. This function is listed in Table 7 and is, of course, limited by the inner field cutoff at $V = 23.5$. The data used here do not go to the tidal radius, so, clearly, our global luminosity function is not quite "global." However, we are confident (see the following section) that the observations extend to a radius which contains most of the cluster mass and that what we have missed is mostly in the form of low-mass stars because of mass segregation. Consequently, our global luminosity function (and the corresponding mass function) are systematically deficient in the lowest mass stars. In practice, this means that we will always tend to underestimate the slope of the global luminosity function. For comparison purposes, inner and outer luminosity functions were constructed by summing over the first six and the last three annuli, respectively. These functions are also given in Table 7 and are plotted in Figure 6. They show that mass segregation has taken place in NGC 5053.

The three luminosity functions in Table 7 were converted into mass functions by applying the 16 Gyr oxygen-enhanced isochrone calculated for M68 (McClure et al. 1987). These

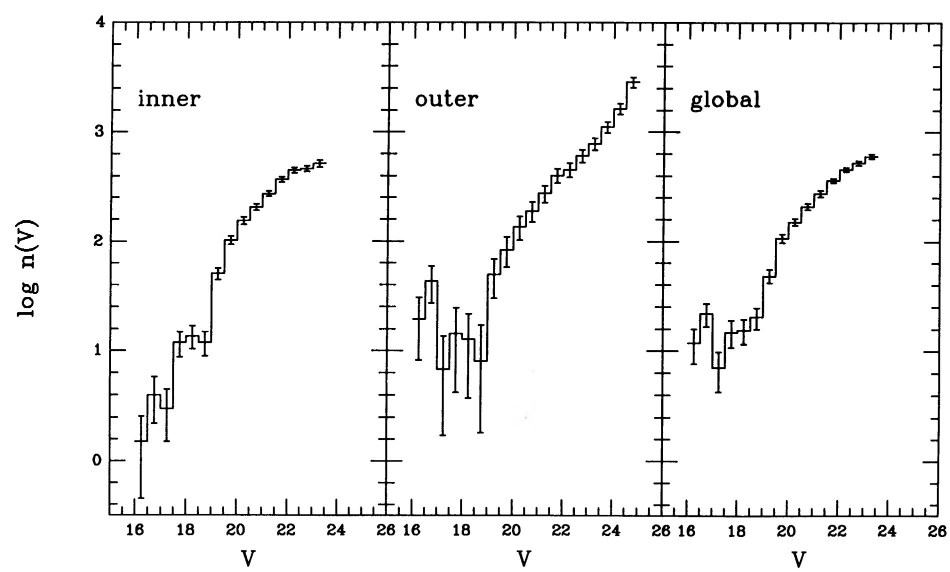

FIG. 6.—Luminosity functions for NGC 5053. The inner region includes the stars within the outer boundary of annulus 5, the outer region includes the stars outside the inner boundary of annulus 8, and the global function is for stars extending throughout the entire area covered by our data. For plotting convenience the luminosity functions have been normalized to a common scale of 1000 stars in the magnitude interval $20 \leq V \leq 22$. The actual numbers of stars may be found in Table 7.

TABLE 8

MASS FUNCTIONS

		GLOBAL		INNER		OUTER	
M_V	m	log $n(m)$	Error	log $n(m)$	Error	log $n(m)$	Error
3.25.....	0.7714	4.87	0.03	4.19	0.03	4.22	0.12
4.25.....	0.7554	4.74	0.03	4.09	0.03	4.14	0.12
4.75.....	0.7342	4.73	0.03	4.06	0.03	4.14	0.09
5.25.....	0.7065	4.75	0.03	4.08	0.02	4.20	0.09
5.75.....	0.6720	4.80	0.02	4.13	0.02	4.28	0.07
6.25.....	0.6341	4.88	0.02	4.20	0.02	4.32	0.06
6.75.....	0.5960	4.94	0.02	4.22	0.02	4.45	0.05
7.25.....	0.5573	4.97	0.02	4.23	0.03	4.53	0.05
7.75.....	0.5173	...	...	...	...	4.69	0.05
8.25.....	0.4688	...	...	...	...	4.71	0.05

TABLE 9

OBSERVED MASS VERSUS $x = 1.5$, $W_0 = 5$ MODEL

V	Observed ($m_\odot$	Model ($m_\odot$)	Observed model
≤20.................	1199	600	2.00
20.0–20.5............	722	651	0.90
20.5–21.0............	967	972	1.00
21.0–21.5............	1229	1308	1.06
21.5–22.0............	1561	1671	1.07
22.0–22.5............	1832	1893	1.03
22.5–23.0............	1985	2065	1.04
23.0–23.5............	2126	2470	1.16

mass functions are listed in Table 8 and shown in Figure 7. Each mass function bin corresponds to a 0.5 mag bin of the luminosity function, with the exception of the first bin, which is for the range $V = 18.0$–19.5. The lines drawn through the calculated mass functions are simply eyeball overlays intended to demonstrate that there are discernible differences. The mass functions can be represented as a power law:

$$n(m) = Am^{-(1+x)}, \quad (1)$$

with the parameter x often referred to as the mass spectral index; A is a normalization constant.

It is clear from Figure 7 that the global mass function of NGC 5053 is close to a power law with $x = 1.5$ over the mass range sampled, i.e., from $0.54 < m/m_\odot < 0.78$. Among the metal-poor globular clusters for which main-sequence mass functions have been determined, NGC 5053 is expected to have suffered the least dynamical evolution. Consequently the slope of the present-day global mass function is most likely to be similar to the initial mass function. It is thus noteworthy that the slope found here is so steep.

A comparison between the observed and predicted mass fractions from an $x = 1.5$ model is given in Table 9. The agreement is quite good except in the first bin, where we observe about twice as much mass as the model predicts. The mass range over this first bin is small, $\Delta m = 0.015\ m_\odot$, and we may simply be seeing an artifact due to the adopted binning and some intrinsic nonuniformity in the cluster mass function over such a small interval. The indicated slopes for the inner and outer mass functions are $x \simeq 0.8$ and $x \simeq 2.0$, respectively.

This degree of mass segregation is broadly consistent with what is found in multimass King models appropriate to NGC 5053—i.e., with a global $x = 1.5$ and a relatively low degree of central concentration. Such models are discussed in more detail below. Here we will consider two extreme models: (1) with a central potential of $W_0 = 3.0$ and a low-mass cutoff of $m_c = 0.03\ m_\odot$ and (2) with $W_0 = 3.5$, $m_c = 0.38\ m_\odot$. Both models contain a number of white dwarfs calculated from an extrapolation of the observed $x = 1.5$ mass function up to 5 $m_\odot$, and both models give an acceptable fit to the projected surface brightness (or star number or mass density) profile. The radial variation of x_{app}, the measured mass spectral index at a particular radius, is shown in Figure 8 for the two models. In both cases, x_{app} was determined from a least-squares fit to the mass spectrum over the mass range $0.38 < m/m_\odot < 0.78$. It can be seen that the degree of mass segregation is smaller in the model with the mass spectrum truncated at 0.38 $m_\odot$. A comparison of the models with the data is shown in Figure 9. The

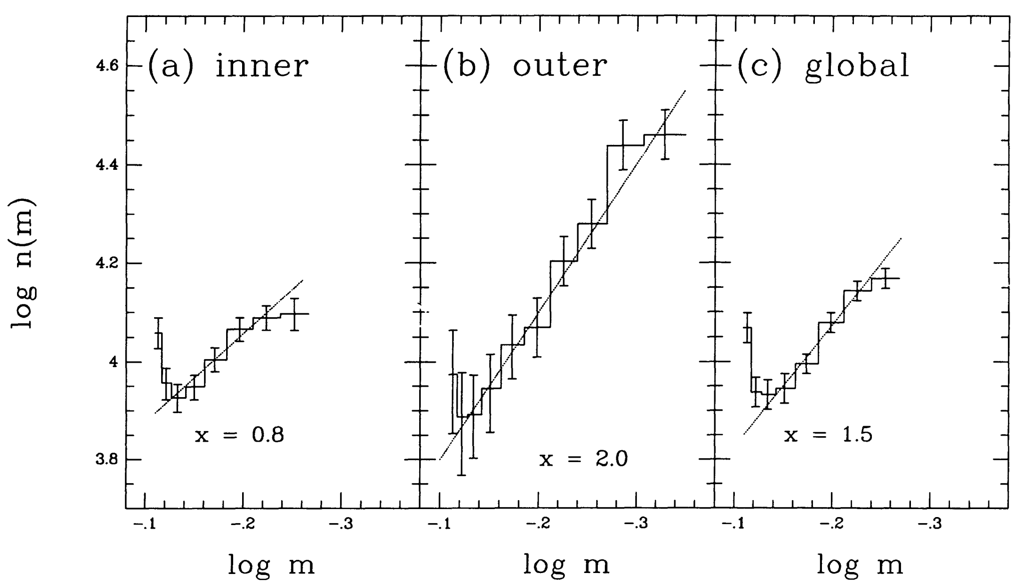

FIG. 7.—Mass functions corresponding to the normalized luminosity functions of Fig. 6. The straight lines correspond to the indicated mass spectral index x for the power law $n(m) \propto m^{-(1+x)}$.

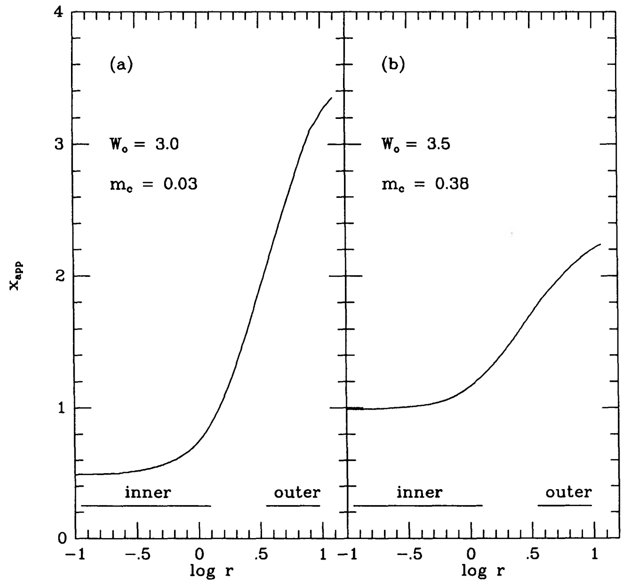

FIG. 8.—Variation of the apparent mass spectral index, x_{app}, with radius for two multimass King models. The central potential, W_0, and the low-mass cutoff, m_c (in solar units), are indicated. The models have a global value of $x = 1.5$. The model locations corresponding to the inner and outer regions shown in Figs. 6 and 7 are also indicated. Model a illustrates the implications of extrapolating the observed mass spectrum into the brown dwarf region, whereas model b assumes that the mass spectrum is truncated at a point corresponding to the observational limit of the data.

differences in the models are obvious, but the data are simply not extensive enough to permit a convincing selection between these two models. This is a sobering result because the two models are very different indeed: model a has 54% of the cluster mass in the form of brown dwarfs ($m < 0.1\ m_\odot$), 6% locked up in white dwarfs, and the observed stars only constitute 9% of the total cluster mass; model b, on the other hand, has 39% of the mass in white dwarfs, and the rest is just the observed stars. Evidently the slight radial variation observed in the mass function does not provide a useful constraint on the low-mass cutoff in NGC 5053. However, as discussed in the following section, the observed velocity dispersion indicates that the cluster has a truncated mass spectrum, similar to that in model b.

7. MULTIMASS KING MODELS

The radial variation of the cluster mass function discussed above is one way to examine the cluster structure. A more familiar equivalent technique is to look at the observed surface brightness or number density profiles for different mass classes. Such data may be conveniently compared with the results of models, computed here following the formalism developed by Gunn & Griffin (1979, hereafter GG). These models are extensions of those first described by King (1986).

The original King models contain just one mass species with an isotropic velocity distribution. They form a single-parameter family of dimensionless models, and in order to fit a specific model to observed data, two scaling parameters must be determined. In general these will involve a length scale and a mass (or luminosity) scale. In contrast, the general multimass King models define much more extended families, since they require the additional specification of how the cluster mass is distributed among the different mass species. One needs high- and low-mass cutoffs together with at least one parameter to describe what happens in between Moreover, these models may include velocity anisotropy, and in that case they will require an additional parameter to specify the radius at which the velocity distribution changes from being predominantly isotropic to predominantly anisotropic. Evidently there are enough knobs to twist that almost any desired surface brightness profile can be tuned in. The observational data can, of course, be used to fix some of the model parameters; e.g., the bright end of the mass spectrum, independent of a fit to, say, the observed surface brightness, and the goodness of fit may constrain others. The most interesting parameters are those related to the dark matter in the cluster: the number and mass of stellar remnants and the low-mass cutoff for the unevolved objects.

One important model constraint is the stellar velocity dis-

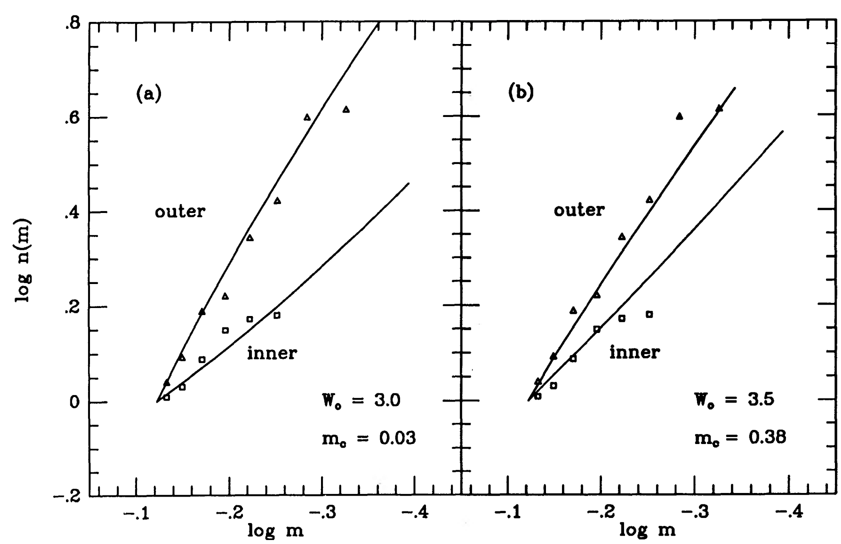

FIG. 9.—Mass segregation in NGC 5053. The two panels correspond to the two models shown in Fig. 8. The data points are the observed mass functions (renormalized to one star in the highest mass bin), with the squares and triangles showing the inner and outer regions, respectively. It is apparent that both models provide a reasonable fit to the observations.

persion. Pryor, (1991) have discussed their velocity measurements of 36 bright giants in NGC 5053. Eight of these stars were easily identified as nonmembers. Three of the remaining 28 stars are considered questionable; one is a velocity variable, and the other two are outliers in the velocity distribution and may be long-period binaries Excluding these stars, the velocity dispersion of the brightest giants in NGC 5053 is $\langle V^2 \rangle^{1/2} \approx 1.4$ km s^{-1}, which is the preferred value. If the two outliers are included, the velocity dispersion rises to $\langle V^2 \rangle^{1/2} \approx 1.8$ km s^{-1}. The fact that just two stars can make such an appreciable difference in the velocity dispersion may be a warning that the sample size is too small to yield a firm result. However, the 36 stars observed are *all* the stars with $V < 15.8$, and so, until fainter stars can be reliably measured, the sample is essentially complete.

For the models discussed here, the main-sequence mass function was assumed to be a power law given by equation (1), with the slope set at $x = 1.5$ in agreement with the observations described earlier. Discrete mass components m_k were used, where m_k is the number-weighted mean mass over the interval Δm defined by the mass bin boundaries. For convenience, the mass bins were chosen to coincide with the magnitude bins used to count the stars. The low-mass cutoff was left as a free parameter, and the mass bins below the last observed mass of this cutoff were set on equal logarithmic intervals to give up to 18 mass components in the models. Remnants from cluster stars which have completed their thermonuclear evolution were also included in most models. These were assigned to two mass bins defined by extrapolating the mass function to 5 $m_\odot$ and to those between 0.8 and 2.0 $m_\odot$. The massive white dwarfs all have $m = 1.01\ m_\odot$, and the others have $m = 0.62\ m_\odot$. No neutron stars were included; the relatively low cluster mass together with the steep mass function and the very low central concentration of NGC 5053 suggest that a significant population of neutron stars is rather unlikely in this cluster.

The data in Table 3 can be used to plot the projected number density of stars in their specific magnitude or mass bins. In addition, we have found it convenient to compare the model output with the projected mass density of the globally visible stars ($V < 23.5$). This profile, computed with the same 16 Gyr isochrone used to determine the mass spectrum, is listed in Table 10. Our profile is in reasonable accord with that published by King et al. (1968). However, our outermost point is a good deal higher than expected for the earlier results. We cannot account for this discrepancy, but it should be noted that the star counts at this radius are based on a very limited spatial sample ($\approx 8\%$ of the whole annulus) in contrast to the photographic work, and are also sensitive to the uncertain background corrections. If our point is really indicating the cluster profile, then, as discussed below, it may indicate a significant degree of anisotropy in the cluster velocity distribution.

Given that our data extend far enough to sample essentially all the cluster mass, it follows that the factors needed to scale the dimensionless multimass King models to the data are easily determined. In particular, for any given model, the scale radius r_s (commonly called the core radius when discussing King models) can be calculated as follows:

$$r_s^2 = \frac{\mathscr{M}_o}{\mu f_m} \frac{f_\sigma}{\sigma_0} . \tag{2}$$

Here $\mathscr{M}_o$ is the observed mass, which, in general, will correspond to the contributions from a limited number of the mass species included in the model; f_m is the fraction of the total mass contained in those mass species; and μ is the dimensionless mass of a King model (cf. King 1966; GG). Note that f_m is determined by the mass function specified and the rule for calculating the remnant population in the model. The observed surface mass density at the cluster center is given by σ_0 and, again, includes contributions from a limited number of mass species; f_σ is the corresponding projected mass density obtained from the model. Similarly, the velocity scale, v_s; needed to convert the model projected velocity dispersions to physical quantities is

$$v_s^2 = \frac{4\pi}{9} \frac{G\mathscr{M}_o}{\mu f_m r_s} . \tag{3}$$

We will discuss only four models which are considered to be representative of the range of possibilities allowed by the currently available data. The defining parameters of each model are listed in Table 11, together with the resulting values for some of the physical quantities which are of interest. These parameters are described in the discussion below. Note that no attempt has been made to fine-tune the input parameters, so that these models are not necessarily the best fits to the data.

7.1. *Isotropic, Complete Main Sequence with Remnants*

This model has a power-law mass function with $x = 1.5$ and includes white dwarf remnants. The mass function extends to a lower cutoff at $m = 0.11\ m_\odot$. This is about the fusion limit for a metal-poor star like those in NGC 5053 (D'Antona 1987). The central potential for this model is $W_0 = 4.0$, and it leads to a scale radius of $r_s = 10.2$ pc. Note that the scale radius does not correspond directly to any measurable quantity. The effective core radius, defined as the radius at which the projected

TABLE 10

PROJECTED DENSITY

Annulus	$\log r_e$ (arcmin)	Mass ($m_\odot$)	$\log \sigma$ ($m_\odot$ arcmin^{-2})	Error
0........	−0.81	80.5	2.724	0.05
1........	−0.57	101.5	2.838	0.05
2........	−0.42	181.1	2.779	0.04
3........	−0.27	355.2	2.772	0.03
4........	−0.12	640.1	2.727	0.02
5........	0.03	808.5	2.588	0.02
6........	0.18	913.5	2.527	0.02
7........	0.33	554.8	2.343	0.02
8........	0.48	262.1	2.052	0.02
9........	0.63	166.9	1.718	0.03
10.......	0.78	81.4	1.054	0.06
11.......	0.92	49.6	0.713	0.10

TABLE 11

KING MODEL PARAMETERS

Parameter	A	B	C	D
W_0	4.0	2.5	3.5	3.5
m_c	0.11	0.11	0.35	0.35
M_t	1.17×10^5	1.18×10^5	4.41×10^4	2.82×10^4
% white dwarfs	12.5	12.4	36.0	0
r_s (pc)	10.2	12.9	9.5	10.1
r_c (arcmin)	1.44	1.47	1.63	1.56
v_s (km s^{-1})	2.85	2.58	2.04	1.59
$\langle v_g^2 \rangle^{1/2}$	2.14	2.48	1.60	1.21

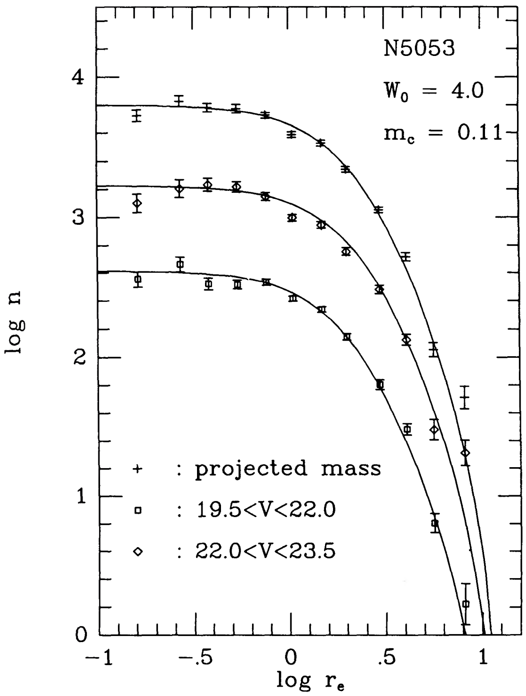

FIG. 10.—Projected density profiles. The solid lines are from a multimass King model characterized by a central potential, $W_0 = 4.0$, and a global mass spectrum of $x = 1.5$, with a cutoff at the hydrogen-burning limit of $m_c = 0.11$ $m_\odot$. The points plotted with open symbols are the projected star counts (per square arcminute) for the indicated magnitude ranges. The data are taken from Tables 6 and 3. The model curve and data points for the range $22 \leq V \leq 23.5$ are offset by 0.5 dex for clarity. The plus signs show the projected mass density for the total number of stars in both magnitude bins. The radial scaling of the model is described in the text. The scaling on the abscissa is determined by adopting a central projected mass density of $\sigma_0 = 10^{2.80}$ $m_\odot$ arcmin^{-2}; see Table 10. Note that the projected mass curve and the data points are offset by 1 dex. The scaling for the other two model curves is fixed by the adopted normalization; there are no adjustable parameters.

number density falls to one-half its central value, is different for each mass species. In this model, the giants have a core radius of $r_c = 6.46$ pc (or 1'.44 at the adopted distance), and their concentration parameter $c = \log r_c/\log r_t$ is $c = 0.982$, where r_t is the tidal radius. The total mass of the model is $\mathcal{M} = 1.17 \times 10^5$ $m_\odot$. The velocity scale is 2.85 km s^{-1}, which leads to a velocity dispersion of 2.20 km s^{-1}.

The comparison of the model with the observed data is shown in Figure 10. The observed projected mass distribution is fairly well fitted by the model, except for the last data point, which is evidently far above the model curve. It should be emphasized that the scaling parameters for this and all subsequent models were computed as described above, and the resulting scaled models were simply overlaid onto the data without further adjustment. The vertical normalization was determined by adopting $\sigma_0 = 10^{2.80}$ $m_\odot$ arcmin^{-2} for the stars with $V \leq 23.5$. The fit to two of the individual mass classes, defined as indicated on the figure, is also shown. The fit to the brighter stars is satisfactory, but for the fainter stars it is somewhat poorer, particularly around the core radius. Since we are comparing an exact $x = 1.5$ model to data which only approximate this slope, some detailed disagreement is not unexpected (cf. model C below).

Models with somewhat smaller values of W_0 give similar results. The models are also fairly insensitive to the-mass cutoff adopted: higher values of m_c lead to essentially indistinguishable models (but with correspondingly smaller total mass and central velocity dispersion), whereas smaller values of m_c, which extend the mass spectrum into the brown dwarf regime, give reasonable fits to the surface brightness distributions even when m_c reaches 0.008 $m_\odot$. However, such extreme models, in which up to 75% of the cluster mass is tied up in brown dwarfs, appear to have more mass segregation than is observed (cf. Fig. 10 and the discussion in the preceding section). In addition, the predicted central velocity dispersion of the giants in such massive clusters is higher than the observed value (Pryor et al. 1991).

7.2. *Anisotropic Model*

The second model examined here is similar to model A (see Table 11) but has an anisotropic velocity dispersion. This model is compared with the observational data in Figure 11. In this case the scale radius was calculated as for an isotropic model, and the fit to the surface brightness profile was used to select the particular model displayed (i.e., the appropriate anisotropy radius). The fit to the data is, if anything, somewhat better than that shown in Figure 10, particularly around the core radius. However, the model was selected primarily because it has an extended envelope, which at least makes the last observed data point appear to be part of the cluster surface brightness distribution. In order to get such a result, the anisotropy radius r_a must be inside the scale radius; for the displayed model $r_a = 0.67 r_s$.

Is such a small anisotropy radius unreasonable? The time scale over which two-body relaxation processes establish isotropy is the deflection time scale t_d, defined by Spitzer (1962, p. 131) as

$$1/t_d = \langle(\Delta v_\perp)^2\rangle / v^2 , \tag{4}$$

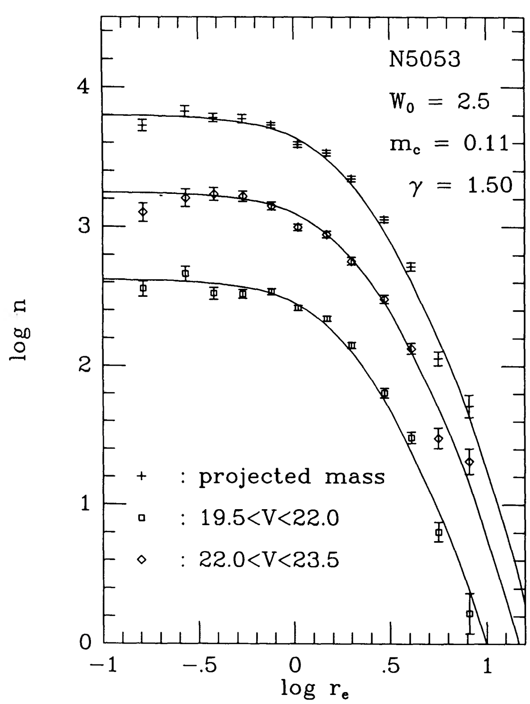

FIG. 11.—Projected density profiles. The data points and model curves are plotted as in Fig. 10. In this case an anisotropic model has been adopted, with $\gamma = r_s/r_a$, where r_s is the scale radius for the model and r_a is the anisotropy radius. This model, unlike the one shown in Fig. 10, fits the outmost data point.

where $(\Delta v_\perp)^2$ is the diffusion coefficient for the transverse velocity component of the *test* population among the *field* population, and v is a characteristic velocity for the test population (see, e.g., Spitzer 1987, pp. 58–62). Following GG, we apply this equation to the multimass case in which a given mass class, denoted by a subscript j, is considered to be the test population interacting with each of the other mass classes, including itself. The speed of the test population will be set to its rms value, $\langle v_j^2 \rangle^{1/2}$, and the diffusion coefficient for an isotropic Maxwellian field population is used. In terms of the model parameters, the deflection time for mass class j is

$$\frac{1}{t_{d,j}} = (18G \ln \Lambda)\left(\frac{\bar{m}}{r_s^2 v_s}\right)\left(\langle u_j^2 \rangle^{-3/2} \sum_k \mu_k \sigma_k h_k\right), \quad (5)$$

where $\ln \Lambda$ is the usual Coulomb term; here $\ln \Lambda = 12$ for all numerical calculations (Spitzer 1987, pp. 58–62). The other symbols are defined as in GG: $\bar{m}$ is the central density weighted mean mass of the stars, u_j is the normalized velocity, v_j/v_s; μ_k is the normalized mass, $m_k/\bar{m}$; σ_k is the normalized density, ρ_k/ρ_0; and h_k represents the stellar dynamics function $\Phi(x) - G(x)$, with $x^2 = (3/2)\langle u_j^2 \rangle / \langle u_k^2 \rangle$, which appears in the diffusion coefficient. The equation reduces to

$$t_{d,j} = 1.05 \times 10^6 (r_s^2 v_s/\bar{m}) \tau_{d,j} \text{ yr}, \quad (6)$$

when the scale radius r_s is expressed in parsecs, v_s in kilometers per second, and $\bar{m}$ in solar masses. The dimensionless term $\tau_{d,j}$ depends only on the normalized model variables and is an increasing function of radius. Note that the central values of $\tau_{d,j}$ is, in general, of order unity, so that the leading terms defines the central deflection time scale. As discussed by GG, it is the *local* value of $\tau_{d,j}$ which is important—the cluster is guaranteed to be isotropic only inside the radius at which the deflection time equals the cluster age. For the specific model under consideration here, $r_s = 12.9$ pc, $v_s = 3.55$ km s^{-1}, $\bar{m} = 0.489\ m_\odot$ and so $t_{d,j} = 1.3 \times 10^9 \tau_{d,j}$ yr. For these low-concentration models, $\tau_{d,j}(0) \approx 3$, so that the central deflection time is rather long at 4.0×10^9 yr. A plot of the deflection time for some of the mass classes in the model is shown in Figure 12. The deflection time at $r/r_s = \frac{2}{3}$ is about 7 Gyr, i.e., close to one-half the nominal age of the cluster. Thus, formally, the cluster is expected to be isotropic at this point. However, it is clearly a close call and in view of the simplifying assumptions and other approximations inherent in this kind of calculation, we conclude that anisotropic models of the kind considered here are not convincingly ruled out by an appeal to two-body relaxation.

7.3. *Observed Mass Function with Remnants*

The third model considered here contains the observed global mass function in 8 bins (corresponding to 0.5 mag intervals in the luminosity function) between the turnoff and 0.54 $m_\odot$. It then continues to 0.35 $m_\odot$ with $x = 1.5$ in 4 more bins. Note that the outer mass function extends to below 0.4 $m_\odot$ (the limit of the available stellar models) at $V = 25.0$, and fainter stars are certainly observed. Thus the truncation at 0.35 $m_\odot$, which corresponds approximately to stars with $M_V = 9.5$, is essentially at the limit of our deepest data. White dwarfs have been included, as in the previous two models, by extrapolating the observed mass function to 5 $m_\odot$. The white dwarfs constitute 36% of the total cluster mass in this model.

The fit to the observed data is shown in Figure 13. The use of the observed mass function instead of the $x = 1.5$ power law

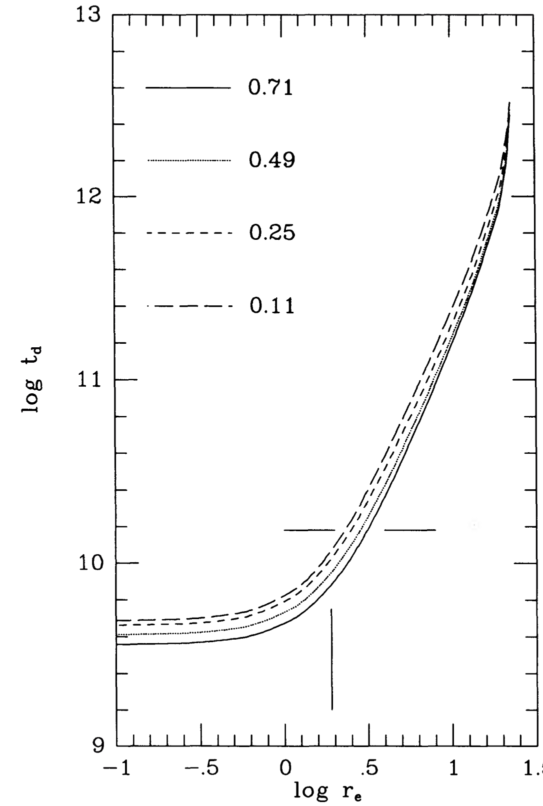

FIG. 12.—Deflection time scale. The deflection time for the anisotropic model of Fig. 11 is plotted as a function of radius for the different mass classes indicated. The vertical line indicates the specified anisotropy radius, and the horizontal lines indicate the nominal age of the cluster, here 15 Gyr. Evidently, the anisotropy radius is within the region which is formally expected to have an isotropic velocity distribution if relaxation processes have been operating for 15 Gyr.

does lead to a small improvement in the fit. Note that this model is essentially the same as model b discussed previously in the context of mass segregation. By truncating the mass function, we have substantially reduced the total mass of the cluster model compared to the previous two models. The projected central velocity dispersion of the giants is predicted to be $\langle v_g^2 \rangle^{1/2} = 1.60$ km s^{-1}. This is somewhat higher than the preferred value.

7.4. *Observed Mass Function, No Remnants*

The final model presented here contains no white dwarfs but is otherwise identical to model C above. This model includes *only* the stars observed to the limit of our data. The fits to the observed surface brightness profiles are shown in Figure 14 and are certainly as good as those of the previous model. The implication is that the present data are incapable of distinguishing between the two cases considered: a cluster with one-third of its mass in the form of white dwarfs and one with no white dwarfs at all.

The predicted central velocity dispersion of the giants in this model is $\langle v_g^2 \rangle^{1/2} = 12.0$ km s^{-1}. The important point to note is that this is the *minimum* value that the cluster can exhibit and still be dynamically consistent with a multimass King model. The global mass-to-visual-light ratio for this model is $\mathcal{M}/L_V = 0.9$.

We recall that the preferred value for the velocity dispersion of the giants is $\langle v_g^2 \rangle^{1/2} = 1.4$ km s^{-1}, a value which falls

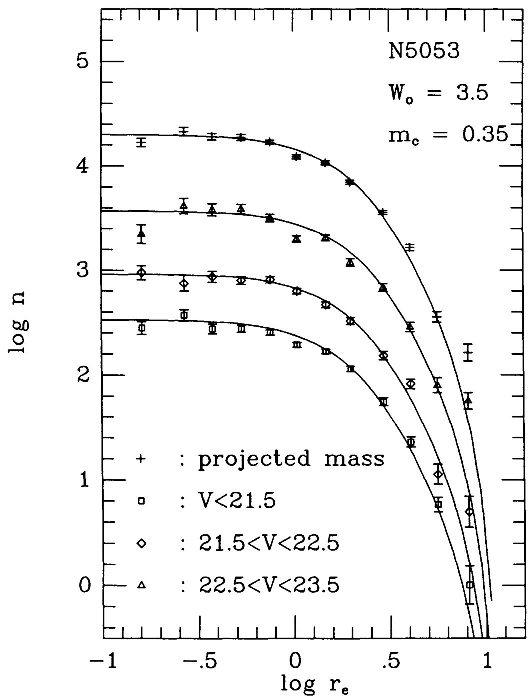

FIG. 13.—Projected density profiles. These plots are similar to Figs. 10 and 11, except that here the observed mass function has been used with a small extrapolation to the cutoff at $m_c = 0.35\ m_\odot$. The model curves are compared with the observations in three magnitude intervals. The indicated scale on the abscissa applies to the brightest points, the other two being offset by 0.5 and 1 dex, respectively. As before, the abscissa scale for the models has been set by the projected mass density, with the corresponding model curve and data points offset by 1.5 dex for clarity.

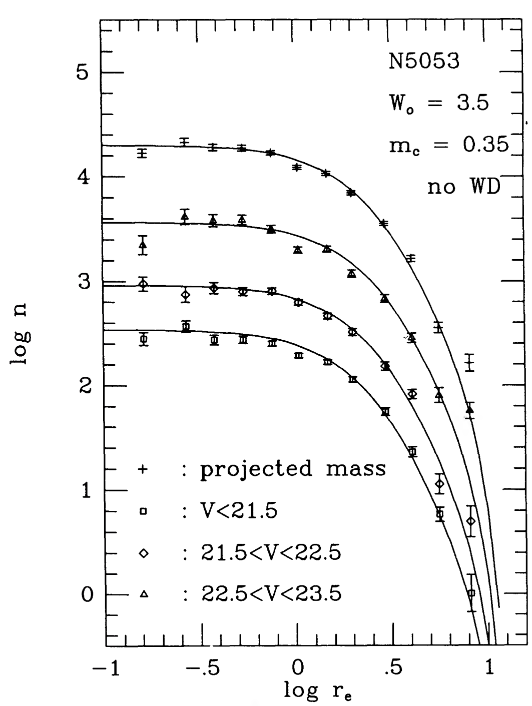

FIG. 14.—Projected density profiles. The model curves and data points have been plotted as in Fig. 13. The only difference here is that this model contains no white dwarfs; it is a comparison based on the observed stars only.

between the predictions of the last two models. From simple scaling arguments, we expect that this observed value for the velocity dispersion will be matched by a model cluster which contains about 34% more mass than model D. A reasonably good model is obtained by simply reducing the number of remnants in model C by 50%. The number of white dwarfs would be further diminished if main-sequence stars with $m < 0.35\ m_\odot$ are present in the cluster. Note, however, that the main-sequence mass function cannot be extended appreciably with the $x = 1.5$ slope, otherwise the predicted velocity dispersion becomes significantly higher than the preferred observational value (cf. model A). Although an appropriate mass-luminosity relationship is not available for the low-metallicity stars in NGC 5053, a comparison with the extended intermediate metallicity models for M13 (Drukier et al. 1988) suggests that the main sequence cannot extend even one more magnitude with the $x = 1.5$ slope of the global mass function. Hence, by an odd coincidence, our observations here extend just deep enough to have observed essentially all the nondegenerate stars in NGC 5053. The predicted truncation of the main sequence must be quite abrupt.

8. SUMMARY AND DISCUSSION

Sstar counts on a set of deep CCD images covering a substantially complete radial cross section of the cluster NGC 5053 have been analyzed. The principle results from this study are the following.

1. A minimum mass-to-visual-light ratio of $\mathcal{M}/L_V = 0.68 \pm 0.07$ has been derived directly from the global luminosity function of the stars with $M_V \leq 9.0$. This value does not depend on kinematical observations or dynamical models of the cluster structure. It is perhaps the best available estimate for the mass-to-light ratio typical of the *luminous* component of an old, metal-poor stellar population.

2. The global mass function for stars in the range $0.78 < m/m_\odot < 0.54$ is well described by a power law: $n(m) \propto m^{(1-x)}$, with $x = 1.5$. In the context of the McClure et al. (1986) correlation, it is noteworthy that the slope is so steep. However, any conclusions drawn from this result must be tempered by (*a*) the fact that the mass range over which the slope has been derived is very small and (*b*) the realization that the other metal-poor clusters with which NGC 5053 may be compared are subject to uncertain corrections due to mass segregation and related dynamical effects.

3. Mass segregation is seen in NGC 5053, but the observed effect is too small to be of much value in constraining the amount of dark matter in the cluster.

4. The projected mass density radial profile has a peculiarly high (compared with an isotropic King model) value in the most distant annulus defined in our study. This may simply be a bad data point, but one cannot conclusively rule out the possibility that the cluster may have an anisotropic velocity distribution which extends inside the nominal core radius.

5. The comparison of our data with multimass King models shows that the observed surface brightness profiles do not provide much leverage for constraining the dark matter. (Essentially, this is equivalent to point 3 above.) Models which extend the main-sequence mass function with the observed $x = 1.5$ slope to the expected end of the hydrogen-burning main sequence predict a central velocity dispersion for the cluster giants which exceeds the preferred observed value of $\langle v_g^2 \rangle^{1/2} = 1.4$ km s^{-1} (Pryor et al. 1991). Indeed, when con-

strained by this velocity dispersion, the models suggest that the cluster does not contain much additional mass beyond what is directly observed. We estimate that only about 20% of the total cluster mass has $V > 25$. This is only about half the amount expected to be in the form of white dwarfs if the initial mass function extended to 5 $m_{\odot}$. Moreover, it implies that the main-sequence mass function suffers a rather abrupt truncation just beyond our observational limit.

The multimass King models with the observed mass function and velocity dispersion for the giants imply a global mass-to-visual-light ratio in NGC 5053 of about $\mathscr{M}/L_V \approx 1.2$. This value, which applies to the whole cluster, is certainly on the low side when compared with other, more centrally condensed clusters (cf. Meylan 1987; Pryor et al. 1989). Interestingly, the only other cluster which appears to have a similarly low $\mathscr{M}/L_V$ value is NGC 5466, which has $\mathscr{M}/L_V \approx 1.1$ (Pryor et al. 1990). NGC 5466 is a low-concentration, low-metallicity cluster very similar to NGC 5053. Pryor et al. (1990) conclude that its mass function must be truncated at an abnormally high value, about $m_c \simeq 0.4$ $m_{\odot}$, to be consistent with the observed velocity dispersion This is an interesting coincidence which is made even more intriguing by the fact that the predicted truncation approximately coincides with the point at which the main-sequence mass functions of a few nearer clusters show dramatic upturns (e.g., Fahlman et al. 1989; Richer et al. 1990). We also note that the mass function of the sparse globular cluster E3 is observed to be truncated at about 0.5 $m_{\odot}$ (McClure et al. 1985) and that the luminosity function of Palomar 5 turns over at about 0.7 $m_{\odot}$ (Smith et al. 1986).

The existence of such striking differences between the mass functions at low stellar masses suggests the following possibilities: (1) that globular star clusters can suffer a significant loss of stars, with a very strong bias toward losing their lowest mass stars, within a Hubble time, or (2) that there is some process which greatly inhibited the formation (or perhaps the initial retention) of very low mass stars in some globular clusters. While the first case is broadly consistent with the idea that low-mass stars are preferentially lost in the course of dynamical evolution (Spitzer 1987, pp. 107–108), it is not at all clear that the evolution of the mass function can be characterized by a low-mass cutoff which marches from low to high mass with time. For example, the evolutionary calculations of Lee, Fahlman, & Richer (1991) do not show such an effect. More realistic and comprehensive calculations are certainly needed to clarify this issue, but it appears that the bias toward losing low-mass stars is simply not great enough to produce a distinct cutoff at the low-mass end of an initially steep power-law mass function. At the present time, it seems much more likely that any deficiency of low-mass stars must be built into the initial mass function. In this case, there is a clear implication that the low-mass stars may constitute a population distinct from the higher mass objects on the upper part of the cluster main sequences. Existing ground-based facilities can probably be pushed to yield at least another magnitude of reliable photometry, and we think it would be of considerable interest to verify the existence of the predicted truncation in both NGC 5053 and NGC 5466.

We thank the Director and Staff of the CFHT for providing the fine telescope and instrumentation which made this work possible. The research of G. G. F. and H. B. R. is supported by operating grants from the Natural Sciences and Engineering Council of Canada. J. N. is supported through a University Research Fellowship provided by NSERC (Canada) and the University of British Columbia.

APPENDIX

THE COLOR-MAGNITUDE DIAGRAM OF NGC 5053

In addition to the five long visual images listed in Table 1, the field 2 data set includes three blue images, each with an exposure of 900 s and mean seeing of about 0\".9. The field is not particularly crowded, and simple aperture photometry produces excellent results. The stars on each frame were measured through an aperture of 5 pixels (1\".0), which optimizes the signal-to-noise ratio for the fainter stars. The photometry of each star on the five v-frames was subsequently averaged (after making small corrections for frame-to-frame offsets caused by the slight variations in the seeing profiles), as were the measurements on the three b-frames. The data for the two colors were then matched giving (v, $b - v$) instrumental magnitudes for each star. These were transformed to the Johnson (V, $B - V$) system in the two-step process. Note that the data were not obtained in photometric conditions, and hence the calibration must be based on stars on the frames.

Eight SKJ stars with photographic photometry were identified on short exposures (60 s) in each color. These stars were used to determine a constant offset ($v - V$) for the visual magnitude and the coefficients c_1 and c_2 in the color equation $(B - Y) = c_1 + c_2(b - v)$. The data are summarized in Table 12. The color coefficient c_2 was found to be 1.274, in good agreement with the standard value published in the CFHT CCD Users Manual. The calibration was then used to determine the magnitudes of the remaining stars on the short frames, and 10 of these stars were, in turn, used to transfer the calibration to the averaged magnitudes and colors of the stars on the long frames. From the residuals of the calibration stars, we estimate the systematic uncertainty in the final magnitudes relative to the SKJ system to be $\sigma_V = \pm 0.04$ and $\sigma_{(B-V)} = \pm 0.04$).

The resulting CMD is shown in Figure 15. This is in fact a composite diagram which includes faint stars measured on the long exposure frames ($V > 17.5$) and the brighter stars from the short frames. Five blue stragglers (Nemec & Cohen 1989) are clearly visible. The main-sequence turnoff and subgiant and giant branches are quite well defined. The horizontal branch is rather sparsely populated, and the reader is referred to SKJ for a more complete look at the morphology of the upper part of the CMD.

A fiducial sequence was constructed for the stars with $V > 19.0$ by defining magnitude bins with a width $\Delta V = 0.25$ mag and determining a medium color for the stars within the bin. For convenience, this fiducial is listed in Table 13. Figure 16 is a plot of the fiducial together with the 100 brightest stars in the field. Also shown are the M92 fiducial sequence from Stetson & Harris (1988) shifted by $\Delta(B - V) = 0.04$ and $\Delta V = 1.48$, and the 16 Gyr, [Fe/H] $= -2.03$, [O/Fe] $= 0.7$ isochrone from McClure et al. (1987),

TABLE 12

PHOTOMETRIC CALIBRATION

Star (SKJ)	V (SKJ)	$B-V$ (SKJ)	V (FRN)	$B-V$ (FRN)
103	15.96	0.90	15.97	0.82
109	16.02	0.75	16.14	0.77
U	16.32	0.69	16.31	0.69
108	16.44	0.72	16.42	0.76
Z	16.61	0.49	16.58	0.50
104	16.71	0.11	16.72	0.08
101	16.72	0.25	16.74	0.15
102	17.24	0.66	17.15	0.71

TABLE 13

NGC 5053 FIDUCIAL SEQUENCE

V	$B-V$	V	$B-V$
19.125......	0.605	21.375......	0.507
19.375......	0.550	21.625......	0.555
19.625......	0.467	21.875......	0.556
19.875......	0.443	22.125......	0.589
20.125......	0.434	22.375......	0.606
20.375......	0.446	22.625......	0.651
20.625......	0.457	22.875......	0.712
20.875......	0.469	23.125......	0.783
21.125......	0.484	23.375......	0.801

which has been shifted by $\Delta(B-V) = 0.08$ and $\Delta V = 16.07$. (The isochrone fits the M92 fiducial almost perfectly.) Finally, the plot also shows a few points from the zero-age horizontal-branch sequence corresponding to the main-sequence isochrone (McClure et al. 1987).

A few comments are in order: (1) The reddening adopted by Stetson & Harris (1988) for M92 is $E(B-V) = 0.02$, and so the comparison in Figure 16 indicates that the isochrone has a zero-point shift of $\Delta(B-V) = 0.02$ and that the reddening of NGC 5053 is $E(B-V) = 0.06$. This is larger than the nominal value of $E(B-V) = 0.01 \pm 0.02$ obtained by SKJ, but, considering the uncertainty in our calibration, we cannot exclude their value. (2) Stetson & Harris (1988) obtained an apparent distance modulus for M92 of $(m-M)_V = 14.60$, and so the offset used in Figure 16 suggests a distance modulus of 16.08 for NGC 5053. This is close to the offset actually used and differs by 0.05 mag from the nominal SKJ value of $(m-M)_V = 16.03$ adopted in the text of our paper. Such a small offset would not affect any of the conclusions drawn there, and, in any case, the difference is not inconsistent with the uncertainty in the calibration. (3) The shape of our fiducial does not quite match the shape of the isochrone, which evidently matches the M92 fiducial almost perfectly. This reason for this mismatch is unclear. (4) The fit of the isochrone to the critical region around the turnoff is excellent, and clearly the M92 giant branch matches our data very well indeed. This comparison (cf. VandenBerg, Bolte, & Stetson 1990) indicates that there is no significant age difference between M92 and NGC 5053. This conclusion is not affected by the uncertainties in the distance modulus or the reddening. (5) The zero-age horizontal-branch models appears to provide an excellent match to the observed points. Hence the magnitude difference between the horizontal branch and the main-sequence turnoff is also consistent with the indicated old age for the cluster.

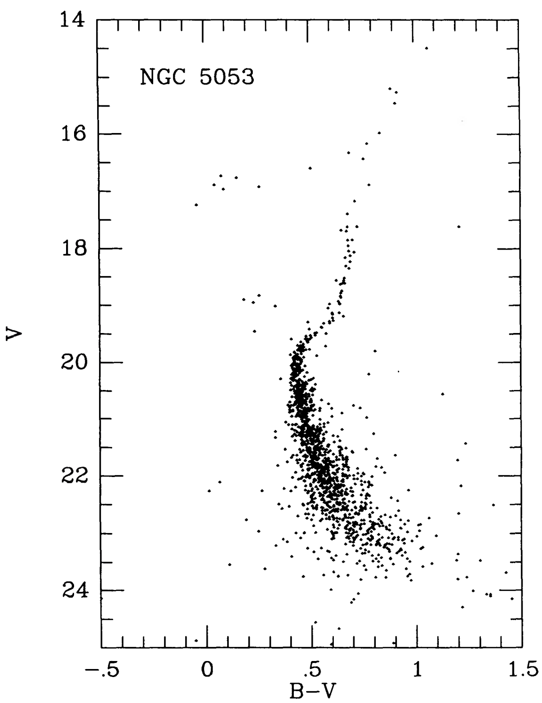

FIG. 15

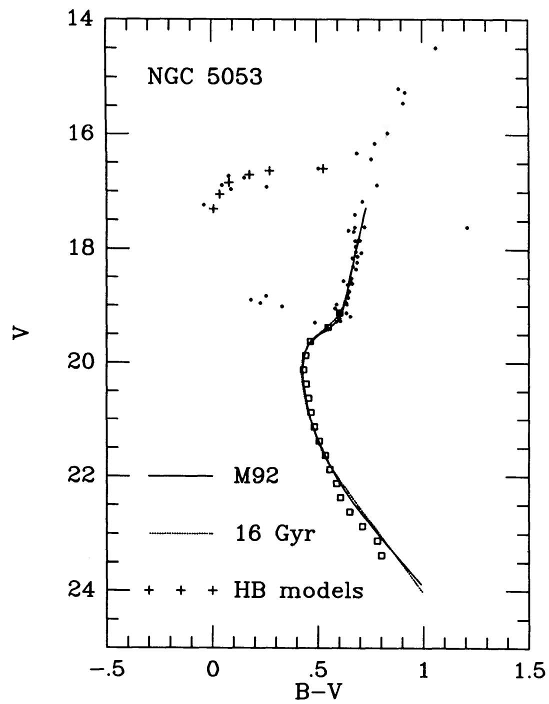

FIG. 16

FIG. 15.—Color-magnitude diagram for NGC 5053. The data are taken from observations in field 2 only.

FIG. 16.—Age of NGC 5053. The fiducial main sequence and subgiant branch ($V \geq 19.0$) of NGC 5053 are shown by the open squares. The brighter stars are plotted as individual points. The M92 fiducial is from Stetson & Harris (1988). The 16 Gyr isochrone is oxygen-enhanced, [O/Fe] = 0.7, and has a metallicity of [Fe/H] = −2.03 (McClure et al. 1987). The zero-age horizontal-branch models are also from McClure et al. (1987).

REFERENCES

Bell, R. A., & Gustafsson, B. 1983, MNRAS, 204, 249
Bolte, M. 1989, ApJ, 341, 168
Chernoff, D. F., & Weinberg, M. D. 1990, ApJ, 351, 121
D'Antona, F. 1987, ApJ, 320, 653
Drukier, G. A., Fahlman, G. G., Richer, H. B., & VandenBerg, D. A. 1988, AJ, 95, 1415
Fahlman, G. G., Richer, H. B., Searle, L., & Thompson, I. B. 1989, ApJ, 343, L49
Gunn, J. E., & Griffin, R. F. 1979, AJ, 84, 752 (GG)
Harris, W. E., & Racine, R. 1979, ARA&A, 17, 241
Iben, I., & Renzini, A. 1983, ARA&A, 21, 271
King, I. R. 1966, AJ, 71, 64
King, I. R., Hedemann, E., Jr., Hodge, S. M., & White, R. E. 1968, AJ, 73 456
Kron, G. E., & Mayall, N. U. 1960, AJ, 65, 581
Lee, H. M., Fahlman, G. G., & Richer, H. B. 1991, ApJ, 366, 455
McClure, R. D., Hesser, J. E., Stetson, P.B., & Stryker, L. L. 1985, PASP, 97, 665
McClure, R. D., VandenBerg, D. A., Bell, R. A., Hesser, J. E., & Stetson, P. B. 1987, AJ, 93, 1144
McClure, R. D., et al. 1986, ApJ, 307, L49
Meylan, G. 1987, in Stellar Evolution and Dynamics in the Outer Halo of the Galaxy, ed. M. Azzopardi & F. Mateucci (Garching: ESO), 665
Murphy, B. W., Cohn, H. N., & Hut, P. 1990, MNRAS, 245, 780
Nemec, J. M., & Cohen, J. G. 1989, ApJ, 336, 780
Nemec, J., Mateo, M., Burke, M., Richer, H. B., & Fahlman, G. G. 1991, in preparation
Peterson, C. J., & King, I. R. 1975, AJ, 80, 427
Piotto, G., King, I. R., Cappacioli, M., Ortolani, S., & Djorgovski, S. 1990, ApJ, 350, 662
Pryor, C., McClure, R. D., Fletcher, J. M., & Hesser, J. E. 1989, AJ, 98, 596
———. 1990, preprint
Pryor, C. Schommer, R. A., & Olszewski, E. W. 1991, in The Formation and Evolution of Star Clusters, ed. K. Janes (San Francisco: ASP), 439
Pryor, C., Smith, G. H., & McClure, R. D. 1986, AJ, 92, 1358
Ratnatunga, K. U., & Bahcall, J. N. 1985, ApJS, 59, 63
Richer, H. B., & Fahlman, G. G. 1987, ApJ, 316, 189
———. 1989, ApJ, 339, 178
Richer, H. B., Fahlman, G. G., Buonanno, R., & Fusi Pecci, F. 1990, ApJ, 359, L11
Richer, H. B., Fahlman, G. G., & VandenBerg, D. A. 1988, ApJ, 329, 187
Sandage, A. R., Katem, B., & Johnson, H. L. 1977, 82, 389 (SKJ)
Smith, G. M., McClure, R. D., Stetson, P. B., Hesser, J. E., & Bell, R. A. 1986, AJ, 91, 842
Spitzer, L. 1962, Physics of Fully Ionized Gases (New York: Interscience)
———. 1987, Dynamical Evolution of Globular Clusters (Princeton: Princeton Univ. Press)
Stetson, P. B. 1987, PASP, 99, 191
Stetson, P. B., & Harris, W. E. 1988, AJ, 96, 909
Suntzeff, N. B., Kraft, R. P., & Kinman, T. D. 1988, AJ, 95, 91
Tyson, J. A. 1988, AJ, 96, 1
VandenBerg, D. A., Bolte, M., & Stetson, P. B. 1990, AJ, 100, 445
Webbink, R. F. 1985, in IAU Symposium 113, Dynamics of Stars Clusters, ed. J. Goodman & P. Hut (Dordrecht: Reidel), 541
White, R. E., & Shawl, S. 1987, ApJ, 317, 246
Zinn, R., & West, M. J. 1984, ApJS, 55, 45